PET-derived amyloid patterns in gray and white matter across the Alzheimer's disease: A high-model-order ICA

Nigar Khasayeva[1,2], Kyle M. Jensen[1], Cyrus Eierud[1], Helen Petropoulos[1], Ruiyan Luo[3], Enrico Premi[4], Barbara Borroni[5,6], Jiayu Chen[1], Vince D. Calhoun[1,2], Armin Iraji[1,2]

[1]Tri-Institutional Center for Translational Research in Neuroimaging and Data Science (TReNDS), Georgia State University, Georgia Institute of Technology and Emory University, Atlanta, GA, USA

[2]Department of Computer Science, Georgia State University, Atlanta, GA, USA

[3]School of Public Health, Georgia State University, Atlanta, GA, USA

[4]Stroke Unit, ASST Spedali Civili, Spedali Civili Hospital, Brescia, Italy

[5]Department of Clinical and Experimental Sciences, University of Brescia, Brescia, Italy

[6]Molecular Markers Laboratory, IRCCS Istituto Centro San Giovanni di Dio Fatebenefratelli, Brescia, Italy

Abstract

Background

Alzheimer's Disease (AD) is a progressive neurodegenerative disorder characterized by gray matter (GM) changes, such as amyloid-beta (Aβ) plaques and neurofibrillary tangles. While GM alterations are well-established, the fine-grained, spatially distinct patterns of homogeneous Aβ uptake and their changes remain poorly understood. Additionally, white matter (WM) pathology is less explored. This study addresses these gaps by leveraging high-model-order independent component analysis (ICA) to identify spatially granular amyloid networks in both GM and WM.

Methods

We analyzed [18F]Florbetapir (FBP) PET images from 716 participants in the Alzheimer's Disease Neuroimaging Initiative (ADNI), classified as cognitively normal (CN), mild cognitive impairment (MCI), or AD dementia. High-model-order ICA was applied to identify 80 GM and 13 WM FBP-related networks, which were labeled using terms from the Neuromark 2.2 Atlas. Statistical analyses assessed diagnostic effects and relationships between these networks and cognitive and neuropsychiatric variables.

Results

Significant diagnostic differences were observed across GM and WM networks, revealing a continuous pattern of change from CN to MCI to AD. The analysis showed that the extended hippocampal, extended thalamic, basal ganglia, and frontal subdomains displayed an MCI profile closer to AD than to CN. In contrast, other subdomains exhibited a more mixed pattern, with MCI sometimes aligning more closely with CN and other times with AD. Notably, the hippocampal–entorhinal complex (HEC) within the extended hippocampal subdomain and the precuneus within the default mode subdomain were consistently associated with cognitive decline, highlighting their roles in disease progression. Additionally, WM networks, particularly the retrolenticular internal capsule (RICap), also demonstrated significant relationships with cognitive measures, suggesting that AD pathology extends beyond GM and disrupts broader network connectivity. These findings were validated in an independent replication dataset.

Conclusion

High-model-order ICA effectively captures distinct fine-grained amyloid distributions, offering a network-level perspective that enhances our understanding of AD neurobiology. By decomposing complex PET signal patterns into distinct networks, this approach underscores the critical role of both GM and WM integrity in AD pathology. The consistent associations of the HEC, precuneus, and WM networks with cognitive decline highlight the widespread impact of AD-related pathology, emphasizing the value of this methodology in advancing AD research.

Introduction

Alzheimer's disease (AD) is a preeminent cause of dementia, characterized by a gradual decline in cognitive functions, including memory, reasoning, and language [1]. It is estimated that approximately 32 million individuals worldwide are affected by AD dementia [2]. Given that the pathological processes underlying AD are believed to commence decades prior to the manifestation of clinical diagnosis [3], it is imperative to elucidate the neurobiological mechanisms that emerge during the prodromal stages of the disease. Mild cognitive impairment (MCI) is recognized as a critical intermediate phase within the Alzheimer's disease course, often representing the initial manifestation of neurodegenerative changes [4]. As an intermediary state between normal aging and dementia, MCI has an annual progression rate of approximately 10–15% to AD dementia [5].

AD pathology has been associated predominantly with gray matter (GM) abnormalities, particularly the aggregation of amyloid-beta (Aβ) plaques and neurofibrillary tangles, widely recognized as hallmark features of AD [6]. However, neuropathological and neuroimaging research has discovered that white matter (WM) degeneration may also be an integral element of AD's pathological cascade rather than mere comorbidity [7]. Studies have shown that WM changes, particularly the degradation of axonal myelin sheaths, are integral to AD and may reflect neurodegenerative processes that emerge early in the disease course, even before significant GM atrophy becomes evident [8]. This emphasizes the necessity of further investigating WM involvement in AD, as it could yield pivotal insights into the disease’s pathophysiology.

Traditional neuroimaging techniques have long been employed to assess structural abnormalities in AD. Methods such as voxel-based morphometry (VBM) [9] and cortical thickness analysis have been the mainstay for detecting GM atrophy [10], while diffusion tensor imaging (DTI) has been crucial in evaluating WM integrity [11]. Although these approaches offer valuable insights into localized anatomical changes, they are limited in capturing the complex network-level interactions of amyloid pathology.

Positron Emission Tomography (PET) has revolutionized the vivo detection of Aβ, providing an invaluable tool for investigating pathological changes from early stages of cognitive decline to advanced cognitive impairment. Amyloid-targeting agents such as [18F]Florbetapir ([18F]FBP) permeate the blood-brain barrier and produce a radioactive signal that is detectable throughout the brain [12]. [18F]FBP is renowned for its high accuracy in detecting Aβ plaques [13]. It has demonstrated its potential in PET studies for identifying uptake variations within the brain in both MCI and AD [14], [15]. A recent study has revealed that [18F]FBP can also identify alterations in WM, particularly the generalized degradation of axonal myelin sheaths [7].

Myelin changes have been associated with cortical Aβ deposition in the preclinical stages of AD [8]. This suggests that PET with [18F]FBP is well-positioned to provide valuable insights into both GM and WM changes in AD.

A widely adopted method for analyzing PET data involves using predefined regions of interest (ROI) to detect variations in tracer uptake [16]. One approach within this methodology requires a neuroanatomically trained expert to manually delineate functional regions for each subject based on their PET images, making it heavily operator-dependent, laborious, and time-consuming. Additionally, tracer uptake in PET imaging does not necessarily conform to predefined anatomical atlases, as some brain regions may exhibit inhomogeneous uptake. These limitations are further compounded by the reliance on ROI-based methods on a fixed number of predefined anatomical regions, which fails to encompass the entire brain space [17]. Another method is voxel-based analysis [18], which evaluates tracer uptake at the individual voxel level, providing a more granular view of tracer distribution across the entire brain space without the need for predefined ROIs, capturing variations that may be overlooked in ROI-based methods. Nevertheless, as a univariate approach, it analyzes each voxel in isolation, potentially overlooking inter-voxel relationships—a limitation it shares with ROI analysis. Additionally, the low signal-to-noise ratio inherent to PET imaging can obscure subtle but meaningful signals. These effects can lead to either underestimation or overestimation of tracer uptake in particular voxels, making it more difficult to detect significant patterns accurately in clinical practice [19]. Additionally, significant patterns may not withstand multiple comparison corrections due to the large number of statistical tests involved. Multivariate data-driven methods present a promising solution to address the abovementioned challenges by integrating information across multiple voxels and identifying spatial patterns that represent regions with similar uptake across individuals. One such method is independent component analysis (ICA), which is used to extract networks that can capture covariance across subjects and reveal discernible differences between different subject groups [20].

Applying ICA to [18F]FBP PET data reveals latent patterns, each representing a distinct spatial distribution of homogeneous Aβ uptake, enhancing our understanding of the neurobiology of AD dementia and providing valuable insights into the differences across the AD course. ICA has been increasingly utilized in the analysis of PET data. In a previous study [21], the authors applied ICA to explore the spatial distributions of Aβ and tau proteins in CN individuals and those with MCI. Their analysis revealed a significant colocalization of Aβ and tau in the default mode network (DMN), indicating that both proteins share similar spatial distribution patterns in this network. Another study [22] employed ICA on [18F]Fluorodeoxyglucose ([18F]FDG) PET data to examine the effects of aging on brain metabolism. This study identified reductions in local metabolic activity in regions such as the bilateral anterior temporal lobe and orbitofrontal cortex, which were found to exert causal effects on other brain regions, including subcortical areas, the inferior frontal cortex, the left temporal cortex, and posterior visual regions. Notably, a separate study [23] utilizing Parallel ICA on both [18F]FDG PET and [11C]Pittsburgh Compound-B ([11C]PiB) PET data in individuals with probable AD identified three networks related to language and visuospatial functions. The networks associated with visuospatial functions closely resembled high-order visual networks and the right hemisphere posterior default mode network. Despite these advancements, previous studies have not yet leveraged high-model-order ICA to study PET data, including [18F]FBP PET, between CN, MCI, and AD.

High-model-order ICA, by increasing the number of independent components, captures more intricate patterns that lower-model-order ICA methods might overlook [24]. This finer decomposition can reveal subtle amyloid variations and refine our understanding of AD neurobiology. In our previous work [25], we applied ICA to [18F]FBP PET data from the Alzheimer's Disease Neuroimaging Initiative (ADNI) cohort to examine group differences between CN and individuals with AD. Our study utilized lower-model-order ICA, which revealed significant group effects in the salience, default mode, and temporal networks. However, we posit that high-model-order ICA could not only capture these established networks but also reveal more intricate and previously unrecognized brain network alterations that may elude lower-order methods.

We applied ICA with a model order of 100 to [18F]FBP PET data to extract PET GM and WM networks and observe differences in tracer uptake were observed between CN, MCI, and AD groups, with a gradient of change across these groups. Furthermore, we performed correlation analyses between these networks and various clinical, cognitive, and neuropsychiatric measures to elucidate their relevance to the symptomatology and progression of AD, which may also offer valuable insights into targeted treatment. This approach not only enhances our understanding of the underlying neurobiological underpinnings of AD but also provides a comprehensive framework for interpreting the cognitive and behavioral impacts of these network patterns.

Materials and Methods

Participants

Data for this research was sourced from the ADNI database (adni.loni.usc.edu). ADNI is a longitudinal study designed to assess whether imaging modalities, such as PET and magnetic resonance imaging (MRI), combined with other biological markers, clinical evaluations, and neuropsychiatric assessments, can be integrated to measure the progression of MCI and early AD [26]. In this study, we focused on [18F]FBP PET imaging due to its established efficacy in capturing beta-amyloid deposition, a key hallmark of AD pathology [13]. This study covers the ADNI-1, ADNI-2, and ADNI-Grand Opportunity (ADNI-GO) phases. The participant eligibility criteria are consistent across the three phases and are comprehensively outlined in the ADNI General Procedures Manual (http://adni.loni.usc.edu/methods/documents/). All participants provided written informed consent.

The dataset comprised 716 PET brain images, including two scans per subject, along with corresponding diagnostic information. Subjects were classified into three groups based on their diagnostic status: controls (N = 293), individuals with MCI (N = 274), and individuals with AD dementia (N = 149). For the primary analysis, one scan per subject was randomly selected, while the second scan was used to assess replicability. To account for potential confounding factors, we applied corrections for site variability, age, and sex. Site correction was performed to mitigate inter-site differences, and only sites with at least 10 subjects were retained for subsequent statistical analyses, yielding a final sample of 624 subjects (Table 1). Age differences between groups were not significant, but given the established age-related nature of AD dementia, age was

included in our correction procedure. Sex showed a significant difference between diagnostic groups and was therefore included in our analysis.

TABLE I. DEMOGRAPHICS OF THE STUDY GROUP AFTER SITE CORRECTION

Diagnostic	N	Sex	N	Age (mean ± SD)
CN	248	Male	104	76.63 ± 8.00
		Female	144	73.81 ± 7.31
MCI	242	Male	142	76.49 ± 7.18
		Female	100	74.68 ± 7.87
AD Dementia	134	Male	70	77.11 ± 8.46
		Female	64	74.07 ± 8.59

CN, cognitively normal; MCI, mild cognitive impairment; AD, Alzheimer's Disease; SD, standard deviation.

Image acquisition and preprocessing

All images were acquired using the [18F]FBP radiopharmaceutical and captured in four 5-minute frames, with slice thicknesses ranging from 1.0 mm to 3.4 mm. T1-weighted MRI scans, with a slice thickness of either 1 mm or 1.2 mm and obtained using a 1.5 or 3 Tesla scanner, were matched with PET images for preprocessing. The initial preprocessing step involved resampling all PET images to a resolution of 2×2×2 mm^3. T1-weighted MRIs were processed using FreeSurfer's recon-all function [27], yielding a skull-stripped brain in both native and fsaverage space. The four 5-minute PET frames were realigned utilizing PETPrep_HMC (https://github.com/mnoergaard/petprep_hmc) and registered to the T1-weighted and fsaverage spaces. Afterward, the four realigned and registered frames were spatially normalized to the MNI305 template [28] and averaged to produce a single motion-corrected PET image for each participant. Then, PET voxel intensities were normalized to standardized uptake value ratios (SUVR) using the cerebellar cortex as the reference region. The cerebellar cortex is frequently employed as a reference region due to the binding of [18F]FBP PET to Aβ plaques, which are notably less prominent in the cerebellum [29]. Finally, the images were smoothed using a 10 mm Gaussian kernel.

Network estimation with high-model-order independent component analysis

ICA is a blind-source separation method [30] commonly utilized to identify spatial covariation patterns by extracting maximally independent components. Unlike principal component analysis (PCA), which operates under assumptions of orthogonality and Gaussian distributions, ICA is predicated on the assumption of non-Gaussianity among sources, making it particularly effective in applications such as PET, where data often represent intricate mixtures of signal and noise [19].

Let $X \in \mathbb{R}^{\{m \times n\}}$ denote the observed PET data matrix, where (m) is the number of voxels and (n) is the number of subjects. ICA assumes that the observed data for subjects, (X), is composed of an unknown linear

mixture of (p) independent sources $S \in \mathbb{R}^{\{p \times m\}}$ and a mixing matrix $A \in \mathbb{R}^{\{n \times p\}}$. The model order (p) determines the number of components extracted by ICA. The mixing matrix, i.e., the loading matrix (A) represents the relative strength of each source contributing to each subject. The objective of ICA is to estimate both the maximally (often assessed using metrics like kurtosis or negentropy) independent sources (S) and the loading matrix (A) such that the observed data can be approximated as $X = AS$ [31].

In our study, we employed a high-model-order ICA model with the number of components set to 100 to capture sources. We first applied dimensionality reduction via PCA to concatenated PET data across all subjects, followed by ICA using the Infomax algorithm [32]. To obtain reliable ICs, we utilized the ICASSO module of Group ICA of fMRI Toolbox [33] (GIFT v4.0c, https://github.com/trendscenter/gift), which runs ICA multiple times using bootstraping and random initialization. ICASSO uses clustering to identify the most stable components as centroids, ensuring reproducibility across iterations [34]. Finally, ICA outputs the spatial sources and their corresponding loadings for subjects (A). In our analysis, we specifically focused on the subject loadings derived from selected sources, i.e., networks, examining how variations in these loadings relate to Aβ accumulation and different stages of cognitive impairment.

[18F]FBP PET networks identification

Out of 100 ICs, we identified GM networks, WM networks, ventricle-related, and artifactual components. We then proceeded with the GM and WM networks, labeling them based on their spatial distribution. GM network labels were assigned according to the Neuromark 2.2 naming convention, a data-driven atlas of canonical brain networks derived from over 100,000 resting-state fMRI datasets, ensuring consistency with its domain and subdomain structure [35], [36]. WM networks were labeled using the JHU white matter atlas [37], which served as an anatomical reference for identifying the spatial distribution of WM networks.

Statistical analysis for cross-group comparison

Linear regression was employed to remove the effects of confounding factors (age, sex, and site) from the high-model-order ICA loading matrix, yielding adjusted loadings that represent the cleaned signals. These adjusted loadings were then analyzed using a two-sample t-test to identify significant differences associated with diagnostic status between the CN, MCI, and AD groups. To account for multiple comparisons, the false discovery rate (FDR) was adjusted using the Benjamini-Hochberg method [38], ensuring robust and reliable results in the identification of significant differences. A significance threshold of $\alpha = 0.05$ was established to determine statistical significance.

Relationship between PET network loadings and cognitive/neuropsychiatric symptoms

We evaluate the effectiveness of our analysis by examining the associations between PET network loadings and cognitive and neuropsychiatric symptoms, as derived from a range of well-established assessments in

the ADNI database. The group effect was removed from both the network loadings and the cognitive and neuropsychiatric scores to ensure that the observed associations reflect meaningful relationships rather than being skewed by group-level variations, thereby avoiding Simpson's paradox [39].

For this analysis, we focused on PET networks that exhibited significant diagnostic differences. By combining MCI and AD subjects (MCI+AD), we then assessed the clinical significance of these networks to identify key disease-related associations, highlighting their diagnostic relevance. These variables include the Alzheimer's Disease Assessment Scale 11-item cognitive subscale (ADAS11) [40] for cognitive evaluation (scores ranging from 0 for no impairment to 70 for maximum impairment), the Clinical Dementia Rating Sum of Boxes (CDRSB) [41] for global assessment of dementia severity (ranging from 0 for no impairment to 18 for severe impairment), the Functional Activities Questionnaire (FAQ) [42] for evaluating daily living activities (ranging from 0 for independence to 30 for maximum dependence), the Mini-Mental State Examination (MMSE) [43] for cognitive assessment (with 30 indicating no impairment and 0 maximum impairment).

Results

Estimated networks across the Alzheimer's disease course

Gray matter networks

Using ICA with a model order of 100, we identified 80 PET GM networks. These GM networks demonstrated spatial correspondence to established GM networks [35], grouped into seven major domains and further categorized into 14 subdomains, including cerebellar (CB), visual-occipitotemporal (VI-OT), visual-occipital (VI-OC), paralimbic (PL), subcortical-extended hippocampal (SC-EH), subcortical-extended thalamic (SC-ET), subcortical-basal ganglia (SC-BG), sensorimotor (SM), higher cognition-insular temporal (HC-IT), higher cognition-temporoparietal (HC-TP), higher cognition-frontal (HC-FR), and the triple network domain: central executive (TN-CE), default mode (TN-DM), and salience (TN-SA) (Figure 1).

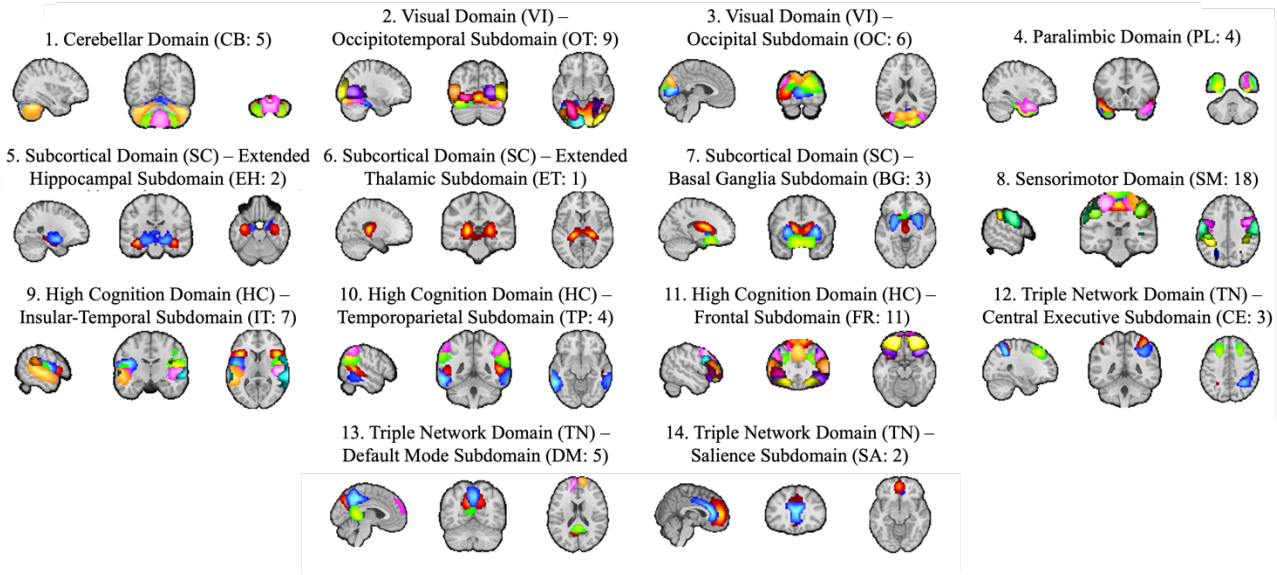

Figure 1. Spatial maps of 80 PET gray matter networks extracted from [18F]Florbetapir PET using independent component analysis, categorized into seven domains and 14 subdomains: 1) Cerebellar, 2) Visual-Occipitotemporal, 3) Visual-Occipital, 4) Paralimbic, 5) Subcortical-Extended Hippocampal, 6) Subcortical-Extended Thalamic, 7) Subcortical-Basal Ganglia, 8) Sensorimotor, 9) Higher Cognition-Insular Temporal, 10) Higher Cognition-Temporoparietal, 11) Higher Cognition-Frontal, 12) Triple Network-Central Executive, 13) Triple Network-Default Mode, and 14) Triple Network-Salience.

Comparison with the fMRI Neuromark 2.2 template showed strong spatial similarity between fMRI and PET networks, particularly in the cerebellar, visual-occipitotemporal, subcortical-basal ganglia, and default mode/salience subdomains (Pearson's $r > 0.6$). Other domains exhibited lower similarity, reflecting more distinct characteristics between [18F]FBP PET and fMRI data.

White matter networks

From the same ICA analysis using a model order of 100, we also identified 13 PET WM networks, each characterized by spatial correspondence to known WM tracts. These networks were assigned to the same domains and subdomains as GM networks, including subcortical domain-retrolenticular internal capsule (RICap), frontal domain-anterior corpus callosum (ACoCa), frontal domain-anterior corona radiata (ACRad), sensorimotor domain-posterior corpus callosum (PCoCa), sensorimotor domain-superior longitudinal fasciculus (SLFas), sensorimotor domain-posterior corona radiata (PCRad), sensorimotor domain-posterior cingulum (PCing), occipitotemporal domain-tapetum (Taptm), occipitotemporal domain-posterior thalamic radiation (PTRad), cerebellar-brainstem domain-anterior middle cerebellar peduncle (AMCbP), cerebellar-brainstem domain-cerebral peduncle (CePed), cerebellar-brainstem domain-corticospinal tract (CSpTr), and cerebellar-brainstem domain-posterior middle cerebellar peduncle (PMCbP) (Figure 2).

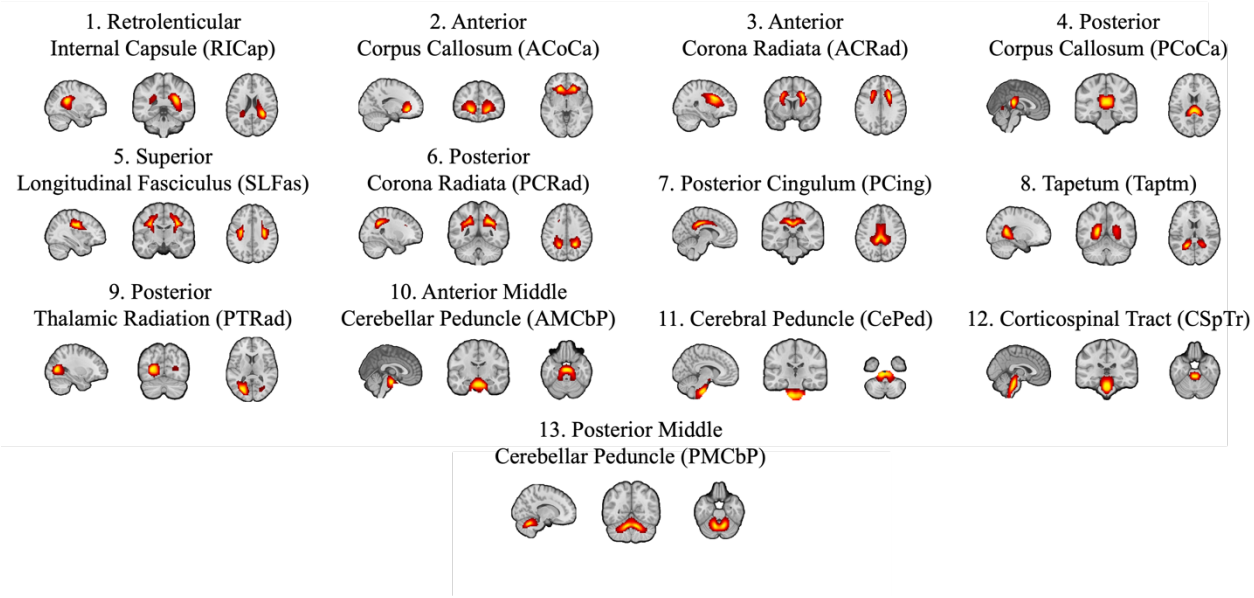

Figure 2. Spatial maps of 13 PET white matter networks extracted from [18F]Florbetapir PET using independent component analysis, including 1) Retrolenticular Internal Capsule, 2) Anterior Corpus Callosum, 3) Anterior Corona Radiata, 4) Posterior Corpus Callosum, 5) Superior Longitudinal Fasciculus, 6) Posterior Corona Radiata, 7) Posterior Cingulum, 8) Tapetum, 9) Posterior Thalamic Radiation, 10) Anterior Middle Cerebellar Peduncle, 11) Cerebral Peduncle, 12) Corticospinal Tract, and 13) Posterior Middle Cerebellar Peduncle.

All identified GM and WM networks exhibited high stability, with ICASSO cluster quality index (Iq) exceeding 0.8.

Cross-group comparison of network loadings

Gray matter networks

The analysis of [18F]FBP PET data included comparisons across seven domains and 14 subdomains, with significant differences identified in numerous GM PET networks. Changes in GM network loadings consistently reflect a systematic transition, with MCI representing an intermediate stage between CN and AD. The three primary comparisons—MCI vs. CN, AD vs. CN, and AD vs. MCI—highlighted distinct patterns of [18F]FBP deposition. The trajectory analysis of our network loadings revealed that the Extended Hippocampal Subdomain, Extended Thalamic Subdomain, Basal Ganglia Subdomain, and Frontal Subdomain predominantly displayed an MCI profile that was closer to AD than to CN. In contrast, other subdomains exhibited a more mixed pattern, with MCI sometimes aligning more closely with CN and at other times with AD.

The most pronounced differences were observed between the AD and CN groups, while the AD vs. MCI and MCI vs. CN comparisons demonstrated fewer, though still notable, distinctions. Specifically, in Figure 3a, 67 networks exhibited significant differences between AD dementia and CN, 58 networks between AD dementia and MCI, and 46 networks between MCI and CN, indicated by a '*' symbol. Of these, 58, 50, and

25 networks, respectively, showed significant effects that persisted in the replicate set, indicated by a '⬥' symbol.

For the MCI vs. CN comparison, the most affected subdomains, with the strongest effect observed in the High Cognition-Frontal Subdomain (Middle Frontal Gyrus, Figure 3b), were followed by the Triple Network-Salience Subdomain, Subcortical-Extended Hippocampal Subdomain, High Cognition-Temporoparietal Subdomain, and Triple Network-Default Mode Subdomain. These subdomains were significant in the discovery set and replicable in the replicate set.

For the AD vs. CN comparison, the most affected subdomains, led by the Triple Network-Salience Subdomain (Medial Prefrontal/Anterior Cingulate Cortex, Figure 3c), were followed by the Visual-Occipitotemporal Subdomain, Subcortical-Extended Hippocampal Subdomain, High Cognition-Frontal Subdomain, High Cognition-Temporoparietal Subdomain, Triple Network-Default Mode Subdomain, and Subcortical-Basal Ganglia Subdomain. These subdomains were significant in the discovery set and in the replicate set.

For the AD vs. MCI comparison, the most affected subdomains, with the greatest effect seen in the Visual-Occipitotemporal Subdomain (Occipitotemporal Cortex, Figure 3d), were followed by the Subcortical-Extended Hippocampal Subdomain, Triple Network-Salience Subdomain, Cerebellar Subdomain, High Cognition-Temporoparietal Subdomain, and Triple Network-Default Mode Subdomain. These subdomains were significant in both the discovery and replicate sets.

Within the Cerebellar subdomain, the anterior cerebellum and vermis show highly significant differences in AD vs. CN and AD vs. MCI ($q < 0.0001$). This indicates these networks are progressively affected as the disease advances from MCI to AD.

Within the Occipitotemporal Subdomain of the Visual Domain, the fusiform gyrus network demonstrated highly significant differences in both AD vs. CN ($q < 0.0001$) and AD vs. MCI ($q < 0.0001$) comparisons, but no significant differences were found in the MCI vs. CN comparison ($q > 0.05$). However, in the medial occipitotemporal cortex—a unique pattern emerged: it showed a significant difference in MCI vs. CN but not in AD vs. CN or AD vs. MCI. In the replication set, this network displayed significant differences across all three comparisons.

Within the Occipital Subdomain of the Visual Domain, the striate cortex and middle occipital gyrus display increasing significance throughout all comparisons as the disease progresses, with remarkably highly significant differences in AD vs. CN and AD vs. MCI ($q < 0.0001$). These patterns indicate that visual processing areas are gradually affected by disease progression.

Within the Paralimbic Subdomain, the anterior lateral temporal cortex exhibits high significance ($q < 0.0001$) across all stages, indicating their critical role in disease progression.

In the Extended Hippocampal Subdomain of the Subcortical Domain, the hippocampal–entorhinal complex showed highly significant differences in all comparisons: MCI vs. CN ($q < 0.0001$), AD vs. CN ($q < 0.0001$), and AD vs. MCI ($q < 0.0001$). The pallidum/hippocampus/amygdala also showed highly significant differences in MCI vs. CN ($q < 0.001$), AD vs. CN ($q < 0.0001$), and AD vs. MCI ($q < 0.0001$). These highly significant differences in all comparisons underscore their major involvement in the disease.

In the Extended Thalamic Subdomain of the Subcortical Domain, the thalamus did not show significant differences in the AD vs. MCI comparison ($q > 0.05$). However, significant differences were observed in the AD vs. CN comparison ($q < 0.01$).

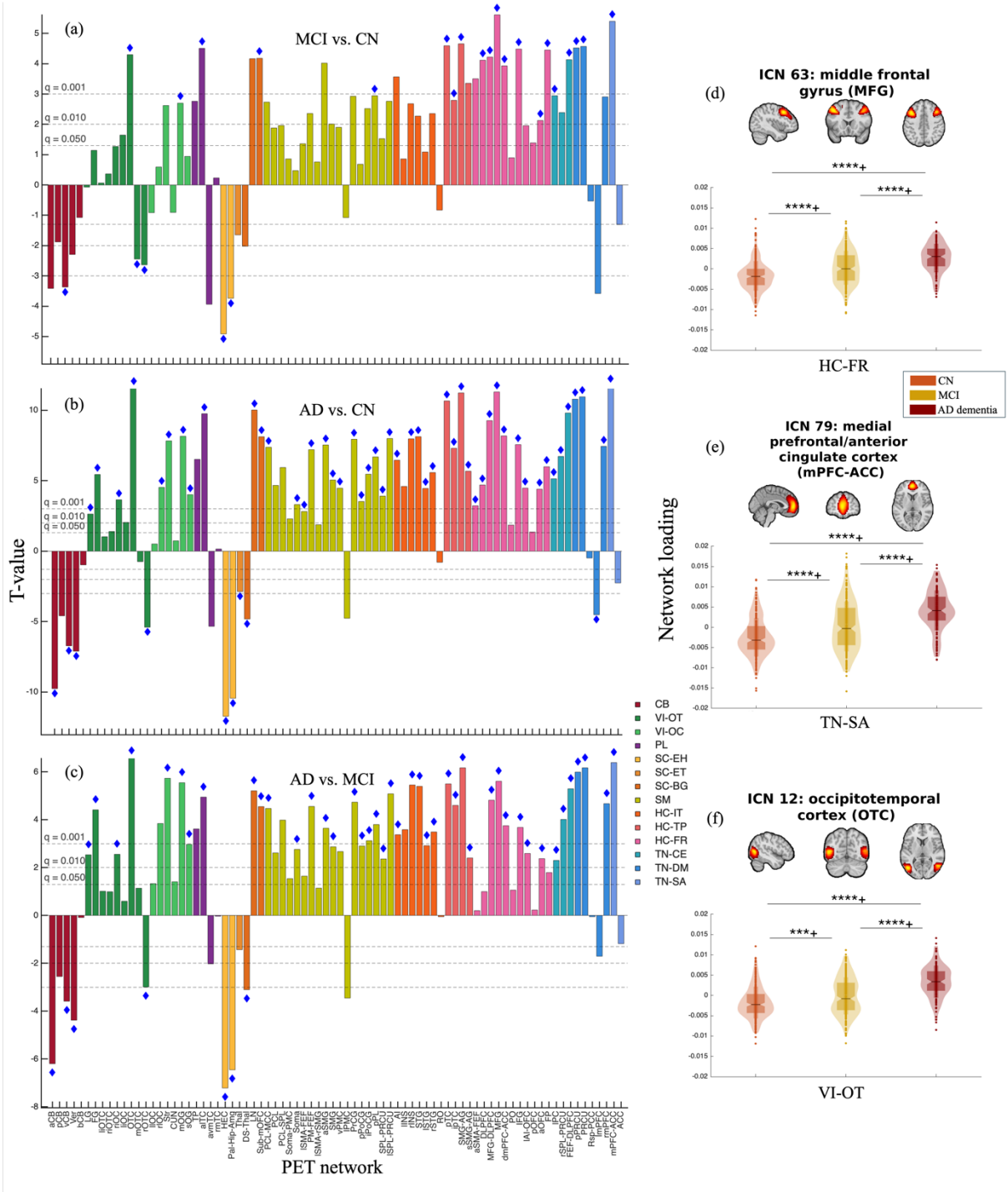

Figure 3. (a, b, c) *Bar plots depicting t-values from two-sample t-tests on adjusted [18F]Florbetapir PET gray matter network loadings, extracted through high-order independent component analysis. The comparisons shown are Mild Cognitive Impairment (MCI) vs. Cognitively Normal (CN), Alzheimer's Disease (AD) vs. CN, and AD vs. MCI, respectively. Significant differences ($q < 0.05$), corrected for false discovery rate (FDR), are marked with star symbols,* (d, e, f) *Violin plots illustrating network loading differences among CN, MCI, and AD groups for the most significantly affected subdomains in each pairwise comparison: HC-FR (High Cognition–Frontal), TN-SA (Triple Network–Salience), and VI-OT (Visual–Occipitotemporal), respectively. ****$q < 0.0001$, ***$q < 0.001$, **$q < 0.01$, *$q < 0.05$, corrected for FDR; ◆ indicates a significant effect in the replicate set.*

Within the Basal Ganglia Subdomain of the Subcortical Domain, the lentiform nucleus network showed significant differences across all comparisons ($q < 0.001$). This consistent involvement in the MCI vs. CN, AD vs. MCI, and AD vs. CN comparisons highlights the lentiform nucleus network as a key player in both MCI and AD stages.

In the Sensorimotor Subdomain, the most striking differences emerged in the paracentral lobule/middle cingulate cortex, precentral gyrus, posterior parietal lobe, and premotor cortex, all showing robust significance in AD vs. CN ($q < 0.0001$) and AD vs. MCI ($q < 0.0001$ to $q < 0.001$). The precentral gyrus and posterior parietal lobe stood out with strong effects across all comparisons, including MCI vs. CN. Meanwhile, the somatosensory cortex, superior parietal lobe, and ventral/lateral premotor cortices exhibited no early-stage differences (MCI vs. CN, $q > 0.05$), but became highly significant in AD vs. CN and AD vs. MCI, reflecting disease progression. Interestingly, the anterior supramarginal gyrus was one of the few regions showing early alterations, with significance even in MCI vs. CN ($q < 0.001$), hinting at its potential role in early dysfunction.

In the Insular-Temporal Subdomain of the High Cognition Domain, the anterior insula and right insula emerged as key regions showing progressive disruption, with strong significance across all comparisons (MCI vs. CN, AD vs. CN, and AD vs. MCI; $q < 0.0001$ to $q < 0.05$). The left insula showed no early-stage differences (MCI vs. CN, $q > 0.05$) but became highly significant in AD vs. CN and AD vs. MCI ($q < 0.0001$, $q < 0.001$), suggesting later-stage involvement. The superior temporal gyrus, particularly its right hemisphere, also exhibited progressive decline, with significance in MCI vs. CN, AD vs. CN, and AD vs. MCI ($q < 0.0001$ to $q < 0.05$), whereas its left counterpart only showed changes at more advanced stages.

Within the Temporoparietal Subdomain of the High Cognition Domain, the posterior temporal cortex network and supramarginal/angular gyrus networks demonstrated highly significant differences in all comparisons ($q < 0.0001$).

Within the Frontal Subdomain of the High Cognition Domain, the middle frontal gyrus/dorsolateral prefrontal cortex, and inferior frontal gyrus across all stages ($q < 0.001$), indicating progressive involvement and critical roles from early MCI to later AD stages.

Within the Central Executive Subdomain of the Triple Network Domain, the frontal eye field/dorsolateral prefrontal cortex demonstrates high significance across all stages ($q < 0.0001$), indicating early and ongoing involvement.

Within the Default Mode Subdomain of the Triple Network Domain, the posterior precuneus and precuneus were both highly significant in all three comparisons: MCI vs. CN ($q < 0.0001$), AD vs. CN ($q < 0.0001$), and AD vs. MCI ($q < 0.0001$), indicating their critical roles from early MCI to AD stages. The left medial prefrontal cortex was significant in MCI vs. CN ($q < 0.001$) and showed high significance in AD vs. CN ($q < 0.0001$), but was not significant in AD vs. MCI ($q > 0.05$).

Within the Salience Subdomain of the Triple Network Domain, the medial prefrontal/anterior cingulate cortex is highly significant across all comparisons ($q < 0.0001$), indicating early and progressive involvement in disease stages.

The overall trends revealed a gradient of changes in GM network loadings from CN to MCI to AD, with specific subdomains and their associated networks showing distinct progression patterns. Notably, the cerebellum, extended hippocampal, and extended thalamic subdomains exhibited predominantly decreased loadings as the disease progressed from CN to MCI to AD. In contrast, other subdomains displayed predominantly increasing patterns with advancing disease stages.

White matter networks

Expanding the analysis to white matter PET networks, similarly, shifts in WM network loadings across the CN, MCI, and AD dementia groups reveal a comparable trajectory, highlighting MCI as a critical intermediate pattern in the gradual decline of white matter integrity. In our white matter analysis, we observed a similar phenomenon in the Frontal Subdomain, where MCI again appeared to be closer to AD than to CN.

We identified 11 networks that differentiated AD dementia from CN and 10 networks that distinguished AD dementia from MCI. Additionally, eight networks showed significant differences between MCI and CN, indicated by a '*' symbol in Figure 4. Overall, seven networks consistently demonstrated differences across all comparisons. Notably, the replication set corroborated most of these significant differences, further validating the robustness of the findings. In Figure 4, a '◆' symbol indicates a significant effect that was replicated in the replicate set, underscoring the reproducibility of WM networks in capturing disease-specific patterns across these diagnostic groups.

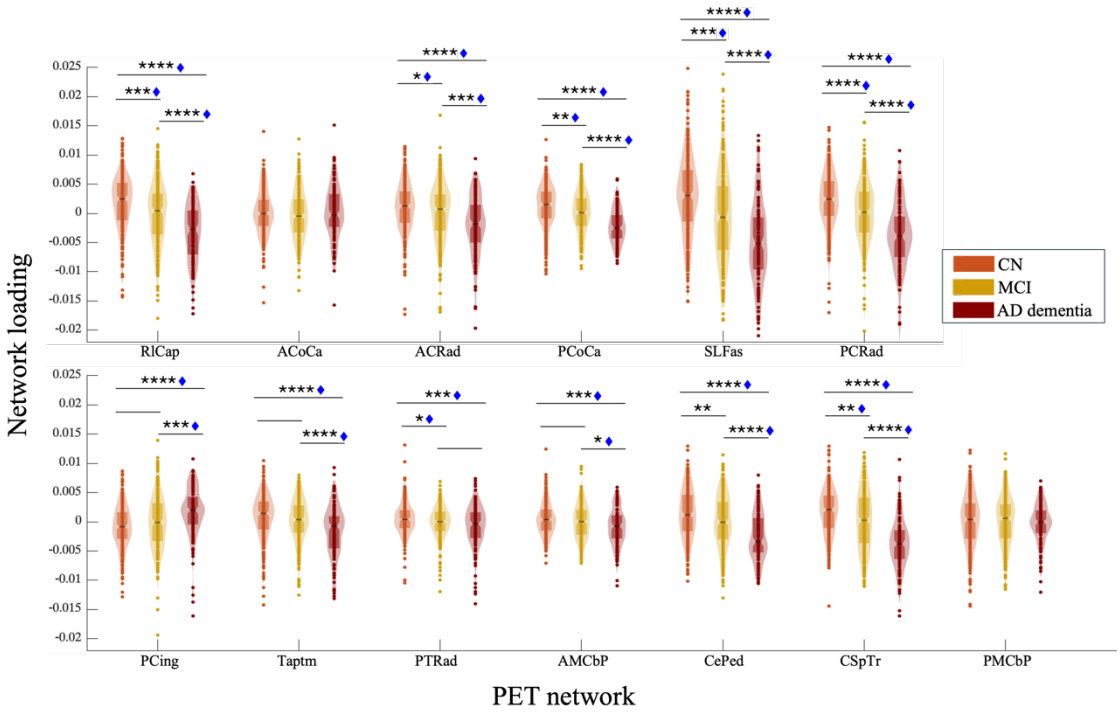

*Figure 4. Violin plots showing PET white matter network loading differences between the three diagnostic groups: cognitively normal (CN), mild cognitive impairment (MCI), and Alzheimer's disease (AD) dementia for Retrolenticular Internal Capsule (RICap), Anterior Corpus Callosum (ACoCa), Anterior Corona Radiata (ACRad), Posterior Corpus Callosum (PCoCa), Superior Longitudinal Fasciculus (SLFas), Posterior Corona Radiata (PCRad), Posterior Cingulum (PCing), Tapetum (Taptm), Posterior Thalamic Radiation (PTRad), Anterior Middle Cerebellar Peduncle (AMCbP), Cerebral Peduncle (CePed), Corticospinal Tract (CSpTr), and Posterior Middle Cerebellar Peduncle (PMCbP). ****q < 0.0001, ***q < 0.001, **q < 0.01, *q < 0.05, corrected for FDR; ◆ indicates a significant effect in the replicate set.*

Association with cognitive and neuropsychiatric variables

Gray matter networks

The correlation analysis was conducted for the MCI+AD group on PET-derived GM networks that exhibited significant diagnostic differences (Figure 5a). ADAS11 scores exhibited the most widespread correlations, spanning the cerebellum domain, subcortical domain—extended hippocampal subdomain, visual domain—occipitotemporal and occipital subdomains, paralimbic domain, sensorimotor domain, high cognition domain—insular-temporal, temporoparietal, and frontal subdomains, and triple network domain—central executive, default mode, and salience subdomains. MMSE scores demonstrated significant associations with the visual domain—occipitotemporal subdomain, subcortical domain—extended hippocampal subdomain, sensorimotor domain, and triple network domain—default mode subdomain. FAQ scores correlated with the subcortical domain—extended hippocampal subdomain and visual domain—occipital subdomain, while CDRSB scores exhibited significant correlations with the subcortical domain—extended hippocampal subdomain.

Among these, the subcortical domain—extended hippocampal subdomain, specifically the hippocampal–entorhinal complex, exhibited consistent significance across all four measures, with ADAS11, MMSE, and CDRSB associations (Figure 5b), which was also replicated in the independent set. Additionally, within the triple network domain—default mode subdomain, the precuneus, and within the sensorimotor domain, the paracentral lobule/middle cingulate cortex, exhibited replicated significance for ADAS11 and MMSE.

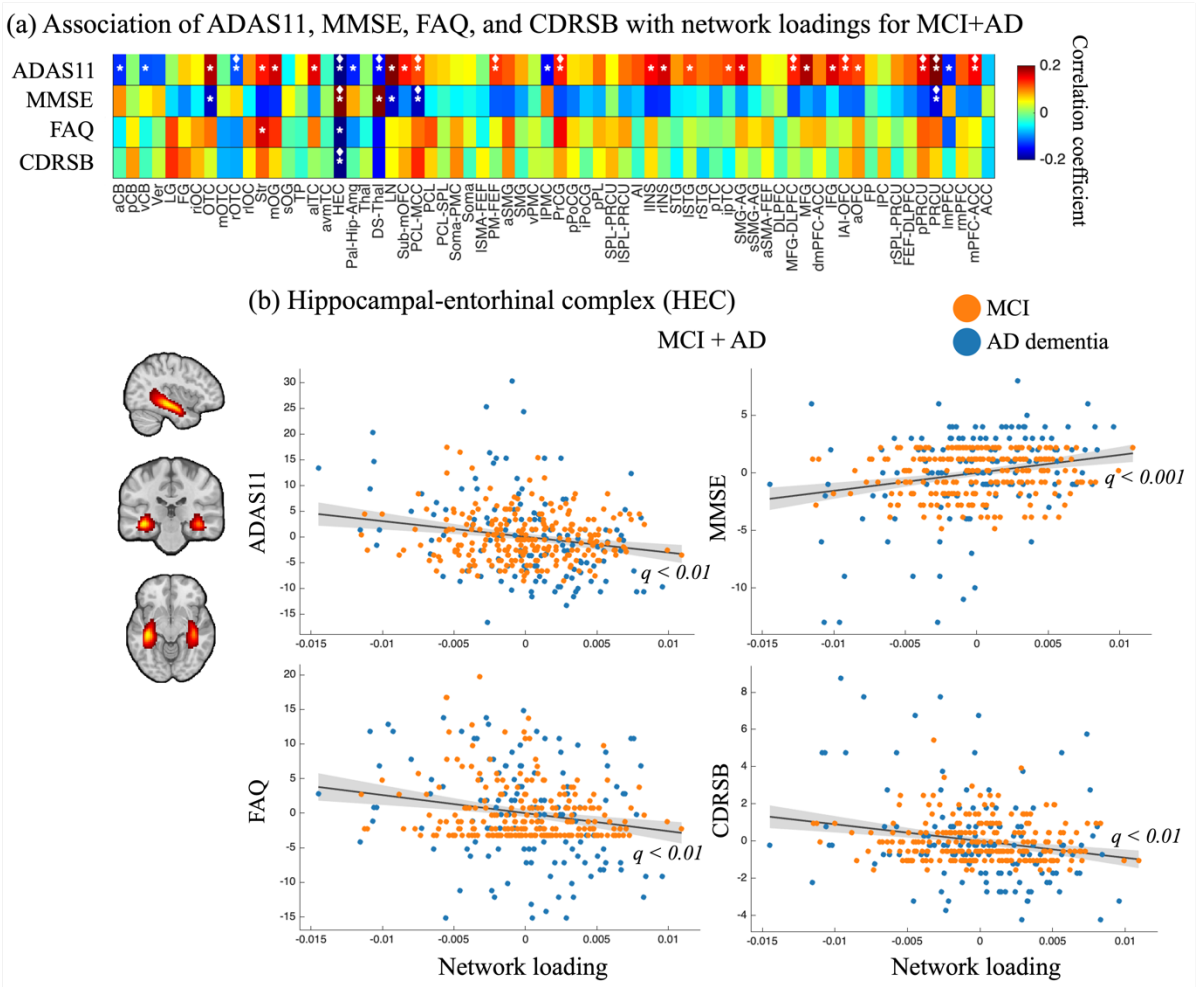

Figure 5. Pearson correlation analysis between standardized PET gray matter network loadings and clinical measures—Alzheimer's Disease Assessment Scale-Cognitive Subscale (ADAS11), Mini-Mental State Examination (MMSE), Functional Activities Questionnaire (FAQ), and Clinical Dementia Rating Sum of Boxes (CDRSB) for the combined group of mild cognitive impairment (MCI) and Alzheimer's disease (AD) dementia. The analysis was performed across all 80 extracted networks. Significant correlations ($q < 0.05$), corrected for false discovery rate (FDR), are marked with star symbols; ◆ indicates a significant effect in the replicate set. (a) Associations between ADAS11, MMSE, FAQ, CDRSB, and network loadings across networks that showed significant group effect, (b) The fitted associations for extended hippocampal subdomain-hippocampal–entorhinal complex (HEC), demonstrating the relationship between network loadings and cognitive scores.

White matter networks

The correlation analysis was also conducted for the MCI+AD dementia group on PET-derived WM networks that exhibited significant diagnostic differences (Figure 6a). ADAS11 scores exhibited the most widespread correlations, spanning the subcortical domain including the retrolenticular internal capsule, the frontal domain including the anterior corpus callosum and the anterior corona radiata, the sensorimotor domain including the posterior corpus callosum and the superior longitudinal fasciculus, the occipitotemporal domain including the tapetum, and the cerebellar-brainstem domain including the anterior middle cerebellar peduncle and the cerebral peduncle. MMSE scores demonstrated significant associations with the subcortical domain including the retrolenticular internal capsule, the frontal domain including the anterior corona radiata, the sensorimotor domain including the superior longitudinal fasciculus and the posterior cingulum, and the cerebellar-brainstem domain including the cerebral peduncle. FAQ scores correlated with the subcortical domain including the retrolenticular internal capsule, the frontal domain including the anterior corpus callosum, the sensorimotor domain including the superior longitudinal fasciculus, the occipitotemporal domain including the tapetum, and the cerebellar-brainstem domain including the cerebral peduncle. CDRSB scores exhibited significant correlations with the subcortical domain including the retrolenticular internal capsule and the sensorimotor domain including the superior longitudinal fasciculus.

Among these, the subcortical domain-retrolenticular internal capsule (Figure 6b) exhibited consistent significance across all four measures with ADAS11, MMSE, and CDRSB associations also replicated in the independent set. The sensorimotor domain - the superior longitudinal fasciculus, also demonstrated consistent associations with all four measures, ADAS11, FAQ, and CDRSB associations were replicated in the independent set.

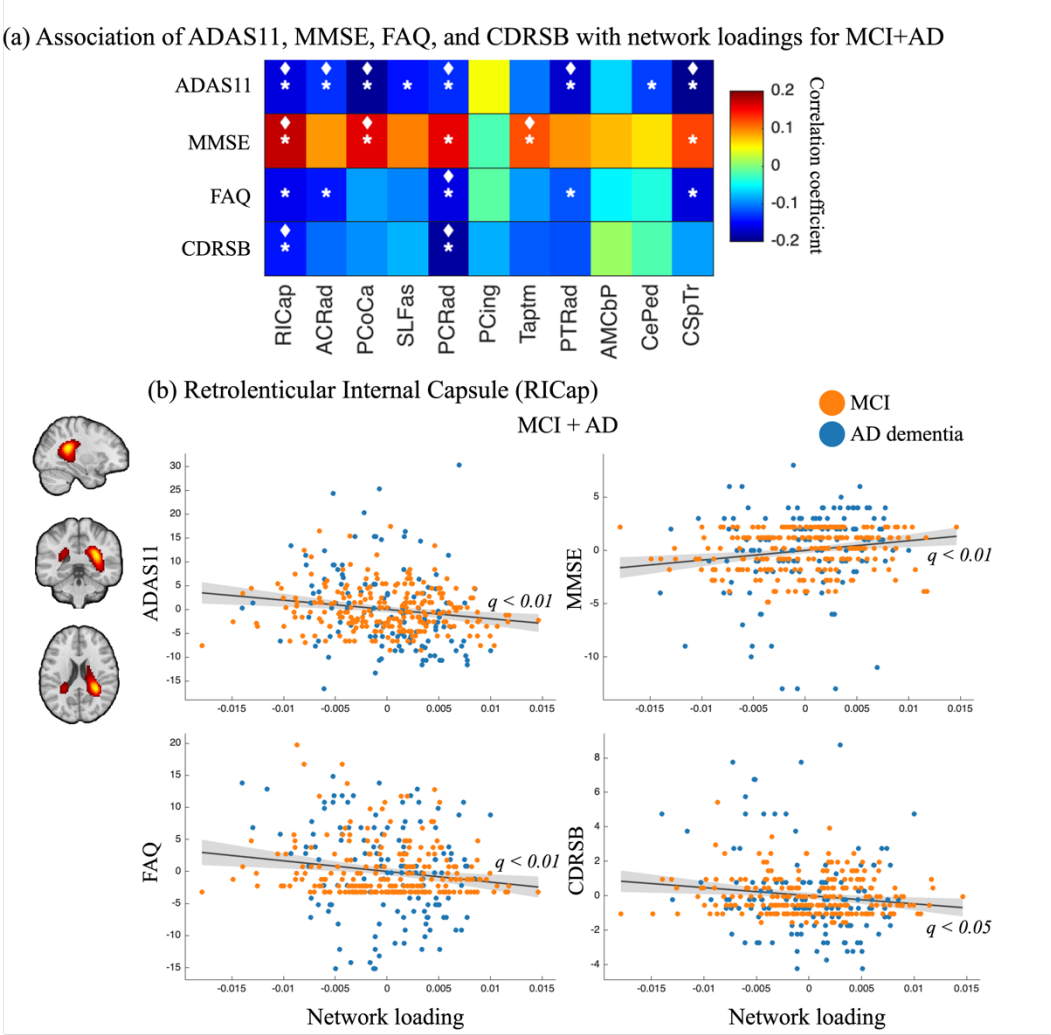

Figure 6. Pearson correlation analysis between standardized PET white matter network loadings and clinical measures—Alzheimer's Disease Assessment Scale-Cognitive Subscale (ADAS11), Mini-Mental State Examination (MMSE), Functional Activities Questionnaire (FAQ), and Clinical Dementia Rating Sum of Boxes (CDRSB) for the combined group of mild cognitive impairment (MCI) and Alzheimer's disease (AD) dementia. The analysis was performed across all 80 extracted networks. Significant correlations (q < 0.05), corrected for false discovery rate (FDR), are marked with star symbols; ◆ indicates a significant effect in the replicate set. (a) *Associations between ADAS11, MMSE, FAQ, CDRSB, and network loadings across all networks,* (b) *The fitted association for the Subcortical subdomain—retrolenticular internal capsule (RICap), demonstrating the relationship between network loading and cognitive scores.*

Discussion

We applied high-model-order ICA to investigate the neurobiological mechanisms underlying AD through the analysis of [18F]FBP PET data. By leveraging ICA, we were able to identify spatially distinct brain networks that may reveal novel insights into the progression of AD, particularly in relation to amyloid deposition patterns and their effects on cognitive function. Our findings emphasize the role of GM and WM alterations in AD pathology, with significant changes observed across several brain regions and domains.

The observed similarity between PET and fMRI networks highlights the preservation of coherence across imaging modalities despite fundamental differences in their underlying physiological signals. While early-phase PET is often used as a proxy for cerebral perfusion and neurodegeneration (akin to FDG-PET), high-order ICA can extract comparable network-level information even from traditional amyloid PET imaging. Interestingly, dual-phase PET using both amyloid and tau tracers [44], [45] has demonstrated that the early phase reliably captures brain patterns closely aligned with FDG-PET, serving as a marker of cerebral perfusion and neurodegeneration. Variability in network correspondence may stem from methodological distinctions, differences in metabolic and functional architecture, or sample characteristics. Nevertheless, the ability of PET networks to recapitulate the established domain and subdomain structure of Neuromark 2.2 underscores the robustness of [18F]FBP PET ICA in delineating meaningful neurobiological networks relevant to AD research.

In the cerebellum domain, highly significant differences were observed in the anterior cerebellum, as well as the vermis, across the AD dementia and CN groups. While often considered peripheral in cognitive research, the cerebellum plays a crucial role in motor coordination, balance, and mental processes such as working memory and attention. Cerebellar amyloid pathology is frequently observed in early-onset AD [46]. Neuropathological studies reveal that amyloid accumulation in the cerebellum primarily occurs during the advanced stages of AD when other cerebral regions are already severely affected [47].

In the visual-occipitotemporal subdomain, significant differences in the fusiform gyrus were observed in AD vs. CN. The fusiform gyrus network, responsible for visual processing, remains relatively unaffected from CN to MCI but shows a marked shift in activity as AD progresses, suggesting that amyloid deposition in these regions occurs primarily in the later stages of cognitive impairment. The VI domain is essential for visual processing, and disruptions here can lead to object recognition, visual memory, and spatial awareness impairments [48], [49].

In the visual-occipital subdomain, we found significant differences in the striate cortex and middle occipital gyrus across all comparisons, including CN vs. MCI, MCI vs. AD, and CN vs. AD, indicating both early involvement and progressive disruption of visual processing regions as the disease advancesIn previous studies, considerable Aβ deposition was observed in the occipital lobes in patients with AD [50], [51], [52]. Research suggests that Aβ accumulation in the occipital lobes in the AD course may be an overlooked marker of an earlier-onset AD or a more aggressive disease course [53]. Given that individuals with occipital amyloid accumulation exhibit visuospatial and visual memory impairments, our findings reinforce the notion that amyloid deposition in the occipital cortex may contribute to AD-related cognitive deficits. The observed progression of significance in visual processing areas suggests that occipital Aβ accumulation, as detected by amyloid PET, should be considered a potential biomarker for tracking disease severity and cognitive decline.

In the subcortical domain, significant differences were noted in the hippocampal–entorhinal complex, thalamus, and lentiform nucleus in basal ganglia. The thalamus is a relay center, playing a crucial role in transmitting sensory and motor signals to the cerebral cortex. Its involvement in cognitive processing and

sleep regulation makes it significant in maintaining attention and consciousness [54]. The basal ganglia structure is involved in motor control, executive decision-making, and reward or aversion-emotional stimulation [55]. In pathologic studies, the presence of amyloid plaques in the striatum, the largest structure of the basal ganglia, predicts a prevalence of dementia and clinicopathological AD [56]. The presence of striatal plaques was also correlated with lower scores on several neuropsychological tests assessing memory [57].

In the high cognition domain, the middle frontal gyrus/dorsolateral prefrontal cortex and inferior frontal gyrus exhibited significant amyloid accumulation across all comparisons, with the most pronounced differences observed in AD dementia vs. CN. This aligns with findings indicating that frontal regions are among the most affected in AD pathology. High cognition-frontal is associated with higher executive functions, such as decision-making, planning, and cognitive flexibility [58]. In AD, a neuropathological staging of different Aβ accumulation phases has been proposed based on post-mortem examinations. The initial stages are marked by significant Aβ deposition in the frontal, parietal, and temporal regions—areas intricately linked to the high cognition domain. Among these, the High cognition-frontal is particularly susceptible to amyloid deposition, making it one of the most affected regions in AD pathology [59].

Within the triple network domain, the posterior precuneus and precuneus exhibited significant differences in AD dementia vs. CN, consistent with research documenting Aβ accumulation and metabolic decline in the default mode network in AD. The default mode is involved in introspective and self-referential processes and has been consistently documented in AD [60]. It has been suggested that Aβ plaques accumulate in brain areas comprising the DMN due to the high metabolic rate of their continuous activation [61]. This accumulation may disrupt neural mechanisms in structures such as the precuneus and posterior cingulate cortex, which are associated with cognitive processes like memory formation and retrieval; disruptions in these processes may underlie AD symptoms [62].

In our study, we observed associations between cognitive decline and disruptions in two key regions: the hippocampal–entorhinal complex and the precuneus. The hippocampal–entorhinal complex, integral to memory encoding and retrieval, has been consistently implicated in the early stages of AD. Similarly, the precuneus—a core region of the default mode network—has been associated with metabolic and connectivity changes observed via MRI and [18F]FDG PET in AD [63], further supporting its role in AD-related cognitive decline. Together, these findings suggest that early network-level disruptions in these regions may serve as valuable biomarkers for tracking disease progression and tailoring therapeutic interventions.

The observed alterations in WM networks align with existing literature emphasizing the critical role of WM integrity in cognitive decline associated with the AD course. Previous studies have reported that WM changes may serve as early indicators of neurodegeneration, often preceding GM atrophy [64]. Our research identified significant differences across the WM networks. Specifically, we found notable diagnostic contrasts across cognitive stages, with pronounced changes in WM networks reflecting the underlying pathophysiology of AD. We identified a particularly strong and replicable effect between CN and MCI in

the posterior corpus callosum (PCoCa). This region has previously been linked to AD, as well as worse cognition [65]. The posterior corpus callosum plays an important role in sensorimotor functions and many cognitive functions, and lesions in the corpus callosum have been previously associated with cognitive impairment [66]. Our results build upon this and suggest that alterations in WM in the PCoCa may be valuable as a potential biomarker that is prominent in the early stages of AD as well as for the different clinical presentations of AD-related pathology [67].

The trajectory analysis of our network-level data revealed that the Extended Hippocampal, Extended Thalamic, Basal Ganglia, and Frontal Subdomains in MCI more closely resembled AD than CN. This finding suggests that even at the MCI stage, these subdomains may already exhibit advanced or accelerated amyloid burden, potentially foreshadowing more severe neurodegeneration in AD. In contrast, other subdomains presented a more mixed pattern, reflecting an intermediate or transitional state in which MCI alternated between alignment with CN and AD. Collectively, these results highlight a heterogeneity in the vulnerability and progression of amyloid pathology across the brain. Some regions—particularly those crucial for memory encoding and executive function—appear to undergo a more rapid transition toward an AD-like phenotype, whereas others follow a more gradual or varied course. This nuanced view underscores the importance of domain-specific analyses in understanding how different brain networks evolve along the AD course.

The white matter findings in the Frontal Subdomain further emphasize that AD-related changes are not confined to gray matter regions. The observation that MCI more closely resembles AD than CN in these frontal white matter networks points to an advanced or accelerated pathological process that can occur in tandem with, or even precede, widespread gray matter alterations. Recognizing this early vulnerability in both gray and white matter networks may prove critical for improving our understanding of AD.

Our application of high-model-order ICA enabled us to dissect [18F]FBP PET data into spatially distinct networks, capturing subtle patterns of amyloid deposition across both GM and WM. By leveraging high-order ICA, we moved beyond conventional region-based or voxel-based analyses to reveal fine-grained, network-level disruptions that are not apparent when examining GM or WM in isolation. For instance, while alterations in GM networks—such as those within the HEC and precuneus—are well-known for their associations with cognitive decline, our approach also revealed distinct WM changes, including in the PCoCa and RICap. Notably, the trajectory of certain MCI subdomains resembling AD rather than CN further underscores ICA's sensitivity in detecting early transitions, capturing disease progression at a more granular level. This dual-level analysis provides a comprehensive picture of AD pathology, reinforcing the potential of high-order ICA not only to confirm established neurobiological alterations in AD but also to expose novel biomarkers that might lead to more targeted therapeutic interventions.

Limitations and Future Work

While PET provides valuable insights, it is not the only imaging modality that can shed light on the complexities of AD dementia [68]. Our findings align with previous fMRI studies that have reported the influence of AD on these networks [69]. Combining PET and fMRI in a multimodal approach can provide a more comprehensive analysis of the AD dementia effects on the brain, providing both anatomic and functional information. This is where the integration of multimodal fusion proves pivotal. As we progress, our research will focus on the application of multimodal ICA to both fMRI and PET data, considering the granular course of AD (preclinical/prodromal and clinical AD) [70] as well as the different clinical presentation of AD-related pathology (logopenic-variant primary progressive aphasia, posterior cortical atrophy, behavioral variant AD and corticobasal syndrome) [71]. This approach will enable us to conduct an exhaustive examination of the changes associated with AD dementia, thereby improving our ability to monitor this disease.

Conclusion

Our findings underscore the power of high-model-order ICA in revealing fine-grained, spatially distinct amyloid deposition patterns in [18F]FBP PET imaging. By disentangling complex PET signals into network-level representations, ICA provides a more nuanced perspective on amyloid burden across both gray and white matter, offering a valuable tool for characterizing AD pathology. This approach demonstrates its potential to capture subtle yet meaningful disease-related changes, reinforcing its relevance for biomarker refinement and disease monitoring.

The diagnostic differences observed across GM and WM networks reveal a continuous and intricate trajectory of amyloid-related changes from CN to MCI to AD, capturing the evolution of pathology. The extended hippocampal, thalamic, basal ganglia and frontal regions suggest that MCI mirrors AD more closely than CN. In contrast, other subdomains display a more mixed pattern, with MCI aligning with CN in some cases and AD in others. Critically, the HEC and precuneus emerge as key regions intimately tied to cognitive decline, echoing their pivotal roles in AD. Beyond GM, the identification of WM PET networks challenges conventional views of amyloid pathology, revealing a broader, network-level cascade of neurodegeneration that extends deep beyond GM.

These findings redefine the perception of amyloid-driven neurodegeneration, highlighting the vast potential of ICA-based network analysis to disentangle the complex pathology of AD. By capturing the spatially granular amyloid networks that drive disease development, this approach paves the way for more sensitive biomarkers and novel therapeutic strategies. Future research incorporating multimodal imaging and longitudinal analyses will be essential for further validating these findings and advancing precision in AD characterization.

References

[1] W. J. Jansen *et al.*, "Prevalence Estimates of Amyloid Abnormality Across the Alzheimer Disease Clinical Spectrum," *JAMA Neurol.*, vol. 79, no. 3, p. 228, Mar. 2022, doi: 10.1001/jamaneurol.2021.5216.

[2] A. Gustavsson *et al.*, "Global estimates on the number of persons across the Alzheimer's disease continuum," *Alzheimers Dement.*, vol. 19, no. 2, pp. 658–670, Feb. 2023, doi: 10.1002/alz.12694.

[3] D. M. Holtzman, J. C. Morris, and A. M. Goate, "Alzheimer's Disease: The Challenge of the Second Century," *Sci. Transl. Med.*, vol. 3, no. 77, Apr. 2011, doi: 10.1126/scitranslmed.3002369.

[4] J.-Q. Li *et al.*, "Risk factors for predicting progression from mild cognitive impairment to Alzheimer's disease: a systematic review and meta-analysis of cohort studies," *J. Neurol. Neurosurg. Psychiatry*, vol. 87, no. 5, pp. 476–484, May 2016, doi: 10.1136/jnnp-2014-310095.

[5] S. T. Farias, D. Mungas, B. R. Reed, D. Harvey, and C. DeCarli, "Progression of mild cognitive impairment to dementia in clinic- vs community-based cohorts," *Arch. Neurol.*, vol. 66, no. 9, pp. 1151–1157, Sep. 2009, doi: 10.1001/archneurol.2009.106.

[6] C. R. Jack and D. M. Holtzman, "Biomarker Modeling of Alzheimer's Disease," *Neuron*, vol. 80, no. 6, pp. 1347–1358, Dec. 2013, doi: 10.1016/j.neuron.2013.12.003.

[7] A. Moscoso *et al.*, "18F-florbetapir PET as a marker of myelin integrity across the Alzheimer's disease spectrum," *Eur. J. Nucl. Med. Mol. Imaging*, vol. 49, no. 4, pp. 1242–1253, Mar. 2022, doi: 10.1007/s00259-021-05493-y.

[8] D. C. Dean *et al.*, "Association of Amyloid Pathology With Myelin Alteration in Preclinical Alzheimer Disease," *JAMA Neurol.*, vol. 74, no. 1, p. 41, Jan. 2017, doi: 10.1001/jamaneurol.2016.3232.

[9] J. L. Whitwell, "Voxel-based morphometry: an automated technique for assessing structural changes in the brain," *J. Neurosci. Off. J. Soc. Neurosci.*, vol. 29, no. 31, pp. 9661–9664, Aug. 2009, doi: 10.1523/JNEUROSCI.2160-09.2009.

[10] V. Julkunen *et al.*, "Cortical Thickness Analysis to Detect Progressive Mild Cognitive Impairment: A Reference to Alzheimer's Disease," *Dement. Geriatr. Cogn. Disord.*, vol. 28, no. 5, pp. 389–397, 2009, doi: 10.1159/000256274.

[11] Y. Assaf and O. Pasternak, "Diffusion Tensor Imaging (DTI)-based White Matter Mapping in Brain Research: A Review," *J. Mol. Neurosci.*, vol. 34, no. 1, pp. 51–61, Jan. 2008, doi: 10.1007/s12031-007-0029-0.

[12] L. Trembath, M. Newell, and M. D. Devous, "Technical Considerations in Brain Amyloid PET Imaging with ^{18}F-Florbetapir," *J. Nucl. Med. Technol.*, vol. 43, no. 3, pp. 175–184, Sep. 2015, doi: 10.2967/jnmt.115.156679.

[13] C. M. Clark *et al.*, "Use of Florbetapir-PET for Imaging," 2011.

[14] S. M. Landau *et al.*, "Measurement of Longitudinal β-Amyloid Change with ^{18}F-Florbetapir PET and Standardized Uptake Value Ratios," *J. Nucl. Med.*, vol. 56, no. 4, pp. 567–574, Apr. 2015, doi: 10.2967/jnumed.114.148981.

[15] Z. Yang, J. W. Kinney, D. Cordes, and The Alzheimer's Disease Neuroimaging Initiative, "Uptake of 18F-AV45 in the Putamen Provides Additional Insights into Alzheimer's Disease beyond the Cortex," *Biomolecules*, vol. 14, no. 2, p. 157, Jan. 2024, doi: 10.3390/biom14020157.

[16] F. T. Sun, R. A. Schriber, J. M. Greenia, J. He, A. Gitcho, and W. J. Jagust, "Automated template-based PET region of interest analyses in the aging brain," *NeuroImage*, vol. 34, no. 2, pp. 608–617, Jan. 2007, doi: 10.1016/j.neuroimage.2006.09.022.

[17] S. Aalto *et al.*, "Reproducibility of automated simplified voxel-based analysis of PET amyloid ligand [11C]PIB uptake using 30-min scanning data," *Eur. J. Nucl. Med. Mol. Imaging*, vol. 36, no. 10, pp. 1651–1660, Oct. 2009, doi: 10.1007/s00259-009-1174-1.

[18] J. Shin, S.-Y. Lee, S. J. Kim, S.-H. Kim, S.-J. Cho, and Y.-B. Kim, "Voxel-based analysis of Alzheimer's disease PET imaging using a triplet of radiotracers: PIB, FDDNP, and FDG," *NeuroImage*, vol. 52, no. 2, pp. 488–496, Aug. 2010, doi: 10.1016/j.neuroimage.2010.04.013.

[19] A. Sanaat *et al.*, “A cycle-consistent adversarial network for brain PET partial volume correction without prior anatomical information,” *Eur. J. Nucl. Med. Mol. Imaging*, vol. 50, no. 7, pp. 1881–1896, Jun. 2023, doi: 10.1007/s00259-023-06152-0.
[20] L. Xu, K. M. Groth, G. Pearlson, D. J. Schretlen, and V. D. Calhoun, “Source-based morphometry: The use of independent component analysis to identify gray matter differences with application to schizophrenia,” *Hum. Brain Mapp.*, vol. 30, no. 3, pp. 711–724, Mar. 2009, doi: 10.1002/hbm.20540.
[21] Yuan Li *et al.*, “Brain network alterations in individuals with and without mild cognitive impairment: parallel independent component analysis of AV1451 and AV45 positron emission tomography,” *BMC Psychiatry*, vol. 19, no. 1, p. 165, Dec. 2019, doi: 10.1186/s12888-019-2149-9.
[22] X. Di *et al.*, “Interregional causal influences of brain metabolic activity reveal the spread of aging effects during normal aging,” *Hum. Brain Mapp.*, vol. 40, no. 16, pp. 4657–4668, Nov. 2019, doi: 10.1002/hbm.24728.
[23] R. Laforce *et al.*, “Parallel ICA of FDG-PET and PiB-PET in three conditions with underlying Alzheimer’s pathology,” *NeuroImage Clin.*, vol. 4, pp. 508–516, 2014, doi: 10.1016/j.nicl.2014.03.005.
[24] A. Iraji *et al.*, “Multi-spatial-scale dynamic interactions between functional sources reveal sex-specific changes in schizophrenia,” *Netw. Neurosci.*, vol. 6, no. 2, pp. 357–381, Jun. 2022, doi: 10.1162/netn_a_00196.
[25] N. Khasayeva *et al.*, “Revealing Alzheimer’s Disease Dementia Patterns in [18F]Florbetapir PET with Independent Component Analysis”, doi: 10.1109/embc53108.2024.10782873.
[26] R. Petersen, M. Clinic, M. Albert, S. DeKosky, D. Salmon, and P. Tariot, “ALZHEIMER’S DISEASE NEUROIMAGING PROTOCOL (ADNI)”.
[27] A. M. Dale, B. Fischl, and M. I. Sereno, “Cortical Surface-Based Analysis”.
[28] A. C. Evans, D. L. Collins, S. R. Mills, E. D. Brown, R. L. Kelly, and T. M. Peters, “3D statistical neuroanatomical models from 305 MRI volumes,” in *1993 IEEE Conference Record Nuclear Science Symposium and Medical Imaging Conference*, San Francisco, CA, USA: IEEE, 1993, pp. 1813–1817. doi: 10.1109/NSSMIC.1993.373602.
[29] C. C. Rowe and V. L. Villemagne, “Brain Amyloid Imaging,” *J. Nucl. Med.*, vol. 52, no. 11, pp. 1733–1740, Nov. 2011, doi: 10.2967/jnumed.110.076315.
[30] N. Correa, T. Adalı, and V. D. Calhoun, “Performance of blind source separation algorithms for fMRI analysis using a group ICA method,” *Magn. Reson. Imaging*, vol. 25, no. 5, pp. 684–694, Jun. 2007, doi: 10.1016/j.mri.2006.10.017.
[31] A. Hyvärinen and E. Oja, “Independent component analysis: algorithms and applications,” *Neural Netw.*, vol. 13, no. 4–5, pp. 411–430, Jun. 2000, doi: 10.1016/S0893-6080(00)00026-5.
[32] A. J. Bell and T. J. Sejnowski, “An Information-Maximization Approach to Blind Separation and Blind Deconvolution,” *Neural Comput.*, vol. 7, no. 6, pp. 1129–1159, Nov. 1995, doi: 10.1162/neco.1995.7.6.1129.
[33] A. Iraji, A. Faghiri, N. Lewis, Z. Fu, S. Rachakonda, and V. D. Calhoun, “Tools of the trade: estimating time-varying connectivity patterns from fMRI data,” *Soc. Cogn. Affect. Neurosci.*, vol. 16, no. 8, pp. 849–874, Aug. 2021, doi: 10.1093/scan/nsaa114.
[34] J. Himberg, A. Hyvärinen, and F. Esposito, “Validating the independent components of neuroimaging time series via clustering and visualization,” *NeuroImage*, vol. 22, no. 3, pp. 1214–1222, Jul. 2004, doi: 10.1016/j.neuroimage.2004.03.027.
[35] A. Iraji *et al.*, “Identifying canonical and replicable multi-scale intrinsic connectivity networks in 100k+ RESTING-STATE FMRI datasets,” *Hum. Brain Mapp.*, vol. 44, no. 17, pp. 5729–5748, Dec. 2023, doi: 10.1002/hbm.26472.
[36] K. M. Jensen, J. A. Turner, V. D. Calhoun, and A. Iraji, “Addressing inconsistency in functional neuroimaging: A replicable data-driven multi-scale functional atlas for canonical brain networks,” Sep. 10, 2024. doi: 10.1101/2024.09.09.612129.
[37] S. Mori, S. Wakana, P. C. M. van Zijl, and L. M. Nagae-Poetscher, *MRI Atlas of Human White Matter*, 1. Aufl. s.l.: Elsevier professional, 2005.

[38] Y. Benjamini and Y. Hochberg, “Controlling the False Discovery Rate: A Practical and Powerful Approach to Multiple Testing,” *J. R. Stat. Soc. Ser. B Stat. Methodol.*, vol. 57, no. 1, pp. 289–300, Jan. 1995, doi: 10.1111/j.2517-6161.1995.tb02031.x.
[39] E. H. Simpson, “The Interpretation of Interaction in Contingency Tables,” *J. R. Stat. Soc. Ser. B Stat. Methodol.*, vol. 13, no. 2, pp. 238–241, Jul. 1951, doi: 10.1111/j.2517-6161.1951.tb00088.x.
[40] J. K. Kueper, M. Speechley, and M. Montero-Odasso, “The Alzheimer’s Disease Assessment Scale–Cognitive Subscale (ADAS-Cog): Modifications and Responsiveness in Pre-Dementia Populations. A Narrative Review,” *J. Alzheimers Dis.*, vol. 63, no. 2, pp. 423–444, Apr. 2018, doi: 10.3233/JAD-170991.
[41] S. E. O’Bryant, “Staging Dementia Using Clinical Dementia Rating Scale Sum of Boxes Scores: A Texas Alzheimer’s Research Consortium Study,” *Arch. Neurol.*, vol. 65, no. 8, p. 1091, Aug. 2008, doi: 10.1001/archneur.65.8.1091.
[42] D. A. González, M. M. Gonzales, Z. J. Resch, A. C. Sullivan, and J. R. Soble, “Comprehensive Evaluation of the Functional Activities Questionnaire (FAQ) and Its Reliability and Validity,” *Assessment*, vol. 29, no. 4, pp. 748–763, Jun. 2022, doi: 10.1177/1073191121991215.
[43] M. F. Folstein, S. E. Folstein, and P. R. McHugh, “‘Mini-mental state,’” *J. Psychiatr. Res.*, vol. 12, no. 3, pp. 189–198, Nov. 1975, doi: 10.1016/0022-3956(75)90026-6.
[44] C. Boccalini *et al.*, “Early-Phase ^{18}F-Florbetapir and ^{18}F-Flutemetamol Images as Proxies of Brain Metabolism in a Memory Clinic Setting,” *J. Nucl. Med.*, vol. 64, no. 2, pp. 266–273, Feb. 2023, doi: 10.2967/jnumed.122.264256.
[45] C. Boccalini *et al.*, “Early-phase 18F-Flortaucipir tau-PET as a proxy of brain metabolism in Alzheimer’s disease: a comparison with 18F-FDG-PET and early-phase amyloid-PET,” *Eur. J. Nucl. Med. Mol. Imaging*, Jan. 2025, doi: 10.1007/s00259-024-07063-4.
[46] H. I. L. Jacobs *et al.*, “The cerebellum in Alzheimer’s disease: evaluating its role in cognitive decline,” *Brain*, vol. 141, no. 1, pp. 37–47, Jan. 2018, doi: 10.1093/brain/awx194.
[47] D. R. Thal, U. Rüb, M. Orantes, and H. Braak, “Phases of Aβ-deposition in the human brain and its relevance for the development of AD,” *Neurology*, vol. 58, no. 12, pp. 1791–1800, Jun. 2002, doi: 10.1212/WNL.58.12.1791.
[48] T. W. James, J. Culham, G. K. Humphrey, A. D. Milner, and M. A. Goodale, “Ventral occipital lesions impair object recognition but not object-directed grasping: an fMRI study,” *Brain*, vol. 126, no. 11, pp. 2463–2475, Nov. 2003, doi: 10.1093/brain/awg248.
[49] J. J. Nassi and E. M. Callaway, “Parallel processing strategies of the primate visual system,” *Nat. Rev. Neurosci.*, vol. 10, no. 5, pp. 360–372, May 2009, doi: 10.1038/nrn2619.
[50] H. Barthel *et al.*, “Cerebral amyloid-β PET with florbetaben (18F) in patients with Alzheimer’s disease and healthy controls: a multicentre phase 2 diagnostic study,” *Lancet Neurol.*, vol. 10, no. 5, pp. 424–435, May 2011, doi: 10.1016/S1474-4422(11)70077-1.
[51] W. E. Klunk *et al.*, “Imaging brain amyloid in Alzheimer’s disease with Pittsburgh Compound-B,” *Ann. Neurol.*, vol. 55, no. 3, pp. 306–319, Mar. 2004, doi: 10.1002/ana.20009.
[52] C. R. Jack *et al.*, “11C PiB and structural MRI provide complementary information in imaging of Alzheimer’s disease and amnestic mild cognitive impairment,” *Brain*, vol. 131, no. 3, pp. 665–680, Mar. 2008, doi: 10.1093/brain/awm336.
[53] J. Hwang *et al.*, “Clinical Implications of Amyloid-Beta Accumulation in Occipital Lobes in Alzheimer’s Continuum,” *Brain Sci.*, vol. 11, no. 9, p. 1232, Sep. 2021, doi: 10.3390/brainsci11091232.
[54] T. J. Torrico and S. Munakomi, “Neuroanatomy, Thalamus,” in *StatPearls*, Treasure Island (FL): StatPearls Publishing, 2024. Accessed: Nov. 11, 2024. [Online]. Available: http://www.ncbi.nlm.nih.gov/books/NBK542184/
[55] C. B. Young, V. Reddy, and J. Sonne, “Neuroanatomy, Basal Ganglia,” in *StatPearls*, Treasure Island (FL): StatPearls Publishing, 2024. Accessed: Nov. 11, 2024. [Online]. Available: http://www.ncbi.nlm.nih.gov/books/NBK537141/

[56] D. R. Thal *et al.*, "[^{18} F]flutemetamol amyloid positron emission tomography in preclinical and symptomatic Alzheimer's disease: Specific detection of advanced phases of amyloid-β pathology," *Alzheimers Dement.*, vol. 11, no. 8, pp. 975–985, Aug. 2015, doi: 10.1016/j.jalz.2015.05.018.
[57] D. S. Wolf, M. Gearing, D. A. Snowdon, H. Mori, W. R. Markesbery, and S. S. Mirra, "Progression of Regional Neuropathology in Alzheimer Disease and Normal Elderly: Findings from the Nun Study:," *Alzheimer Dis. Assoc. Disord.*, vol. 13, no. 4, pp. 226–231, Oct. 1999, doi: 10.1097/00002093-199910000-00009.
[58] R. M. El-Baba and M. P. Schury, "Neuroanatomy, Frontal Cortex," in *StatPearls*, Treasure Island (FL): StatPearls Publishing, 2024. Accessed: Nov. 11, 2024. [Online]. Available: http://www.ncbi.nlm.nih.gov/books/NBK554483/
[59] H. J. Aizenstein *et al.*, "Frequent Amyloid Deposition Without Significant Cognitive Impairment Among the Elderly," *Arch. Neurol.*, vol. 65, no. 11, p. 1509, Nov. 2008, doi: 10.1001/archneur.65.11.1509.
[60] M. Grieder, D. J. J. Wang, T. Dierks, L.-O. Wahlund, and K. Jann, "Default Mode Network Complexity and Cognitive Decline in Mild Alzheimer's Disease," *Front. Neurosci.*, vol. 12, p. 770, Oct. 2018, doi: 10.3389/fnins.2018.00770.
[61] R. L. Buckner, J. R. Andrews-Hanna, and D. L. Schacter, "*The Brain's Default Network*: *Anatomy, Function, and Relevance to Disease*," *Ann. N. Y. Acad. Sci.*, vol. 1124, no. 1, pp. 1–38, Mar. 2008, doi: 10.1196/annals.1440.011.
[62] H. Jahn, "Memory loss in Alzheimer's disease," *Dialogues Clin. Neurosci.*, vol. 15, no. 4, pp. 445–454, Dec. 2013, doi: 10.31887/DCNS.2013.15.4/hjahn.
[63] K. Mevel, G. Chételat, F. Eustache, and B. Desgranges, "The Default Mode Network in Healthy Aging and Alzheimer′s Disease," *Int. J. Alzheimer's Dis.*, vol. 2011, no. 1, p. 535816, Jan. 2011, doi: 10.4061/2011/535816.
[64] C. D. Mayo, E. L. Mazerolle, L. Ritchie, J. D. Fisk, and J. R. Gawryluk, "Longitudinal changes in microstructural white matter metrics in Alzheimer's disease," *NeuroImage Clin.*, vol. 13, pp. 330–338, 2017, doi: 10.1016/j.nicl.2016.12.012.
[65] A. Garnier-Crussard, F. Cotton, P. Krolak-Salmon, and G. Chételat, "White matter hyperintensities in Alzheimer's disease: Beyond vascular contribution," *Alzheimers Dement.*, vol. 19, no. 8, pp. 3738–3748, Aug. 2023, doi: 10.1002/alz.13057.
[66] W. M. Freeze *et al.*, "Corpus callosum lesions are associated with worse cognitive performance in cerebral amyloid angiopathy," *Brain Commun.*, vol. 4, no. 3, p. fcac105, May 2022, doi: 10.1093/braincomms/fcac105.
[67] J. S. Phillips *et al.*, "Greater white matter degeneration and lower structural connectivity in non-amnestic vs. amnestic Alzheimer's disease," *Front. Neurosci.*, vol. 18, p. 1353306, 2024, doi: 10.3389/fnins.2024.1353306.
[68] P. N. E. Young *et al.*, "Imaging biomarkers in neurodegeneration: current and future practices," *Alzheimers Res. Ther.*, vol. 12, no. 1, p. 49, Dec. 2020, doi: 10.1186/s13195-020-00612-7.
[69] F. Agosta, M. Pievani, C. Geroldi, M. Copetti, G. B. Frisoni, and M. Filippi, "Resting state fMRI in Alzheimer's disease: beyond the default mode network," *Neurobiol. Aging*, vol. 33, no. 8, pp. 1564–1578, Aug. 2012, doi: 10.1016/j.neurobiolaging.2011.06.007.
[70] C. R. Jack *et al.*, "Revised criteria for diagnosis and staging of Alzheimer's disease: Alzheimer's Association Workgroup," *Alzheimers Dement. J. Alzheimers Assoc.*, vol. 20, no. 8, pp. 5143–5169, Aug. 2024, doi: 10.1002/alz.13859.
[71] J. S. Phillips *et al.*, "Longitudinal progression of grey matter atrophy in non-amnestic Alzheimer's disease," *Brain J. Neurol.*, vol. 142, no. 6, pp. 1701–1722, Jun. 2019, doi: 10.1093/brain/awz091.